(Received 1 April 2025, Accepted 26 May 2025, Scheduled 16 June 2025)

Spin Decoupling-Scalar Holographic Impedance Hybrid Metasurface for Bidirectional Multibeams

Hui-Fen Huang* and Fuhua Liu

School of Electronic and Information Engineering, South China University of Technology, Guangzhou, China

ABSTRACT: This paper proposes a spin decoupling phase gradient (SDPG)-scalar holographic impedance (SHI) bidirectional hybrid metasurface (MTS). The integrated SDPG MTS modulates the space wave (SPW) and is excited by the horn, whereas the SHI-integrated MTS modulates the surface wave (SFW) and is excited by a surface-mounted monopole. As example, (1) Dual orbital angular momentum (OAM) beams are generated at 18.3 GHz by the integrated SDPG MTS at 18.3 GHz: left hand circular polarization (LHCP) (OAM mode l_1= 1, $\theta_1 = 30^\circ$, $\varphi_1 = 0^\circ$), right hand circular polarization (RHCP) ($l_2 = -1$, $\theta_2 = -30^\circ$, $\varphi_2 = 0^\circ$). (2) Linear polarization (LP) pencil beam is generated at 7.8 GHz by the integrated SHI MTS: ($l_3 = 0$, $\theta_3 = -150^\circ$, $\varphi_3 = 0^\circ$). The peak gain is 19.9 dBi, and the OAM purity is above 84.7%. The novelty of the manuscript is as follows: (1) To the authors' knowledge, a full-space SDPG-SHI hybrid metasurface has been developed for the first time, which greatly expands the bidirectional multifunctional design freedom. (2) Much higher aperture efficiency (AE) than published results. (3) The proposed SDPG-SHI hybrid MTS simultaneously possesses the following advantages: small size ($\pi \times 719\lambda \times 719\lambda$ at 18.3 GHz, and $\pi \times 306\lambda \times 306\lambda$ at 7.8 GHz), full space, multibeams, multipolarization, reconfigurability, and simultaneous modulation of SPW and SFW. The developed MTS has promising applications in high-capacity bidirectional communication scenarios.

1. INTRODUCTION

MTS, with the advantages of low profile and easy fabrication, can provide functionalities beyond those obtained by conventional devices. There are two kinds of MTSs: phase modulation (manipulating spatially propagating waves) [1–9] and impedance modulation (manipulating surface waves) [10–12]. There are two types of phase modulations: propagation phase and Pancharatnam-Berry (PB) phase, both of which alone cannot control any pair of orthogonal polarizations and limit the multifunctional design freedom. Spin decoupling MTS, integrating both PB phase and propagation phase, provides a good solution [1]. There are two types of impedance modulations: scalar and tensor impedances. Tensor impedance MTS can simultaneously control beam direction, polarization, and OAM mode with high AE, and attracts much more attention than SHI MTS [13]. Scalar impedance surfaces generally support either TM or TE surface wave modes. Most of the SHI unit cells are designed on a grounded substrate, and the dominant surface wave mode is TM type no matter whether the unit cells are capacitive or inductive [14, 15]. The conventional TM mode SHI MTS has low AE ($< 10\%$) due to the utilization of a single polarization [16, 17]. So this paper proposes a high AE TM mode SHI MTS.

Multifunction devices are essential for modern integrated systems and miniaturization. Active reconfigurable metasurfaces can achieve multifunctionality and miniaturization but at the cost of complex design, energy loss, and high costs. Consequently, numerous multifunctional passive MTSs have been developed, such as those enabling polarization control, wavelength multiplexing, OAM mode manipulation, spatial multiplexing, or simultaneous multiplexing of multiple physical quantities [18]. However, these existing multifunctional MTSs are typically composed of a single type of unit — such as SHI MTS, tensor holographic impedance MTS, or phase modulation MTS alone. Recently, hybrid MTSs (integrating two or more types of units) have been proposed and significantly enhance the design flexibility for multifunctional applications, such as spin-decoupled MTSs [19], SHI-reflection phase hybrid MTSs [20], and SHI-THI hybrid MTSs [21]. However, the works for hybrid MTS are limited.

The above mentioned MTSs only function in half space. In order to enlarge the beam coverage and increase the spatial efficiency, full space MTSs works have been developed: A transmission-reflection integrated full-space MTS with three layers [22], a bidirectional TE mode SHI MTS with AE 26% [23], and a bidirectional SHI MTS supporting both TE and TM modes with total AE 33.9% [16].

According to the above research background, the following conclusions are obtained: (1) Hybrid MTSs meet the demand for modern integrated systems and miniaturization. (2) Full space MTSs can enlarge the beam coverage and increase the spatial efficiency. However, to the knowledge of the authors, the published full space MTSs are phase or surface impedance modulation alone, and there is no full space SPW-SFW hybrid MTS. This paper develops a full space SDPG-SHI hybrid MTS. The highlights of this paper are as follows: (1) For the first time, a single layer full space surface wave-space wave hybrid MTS is provided. (2) Much higher TM mode SHI AE than published

* Corresponding author: Hui-Fen Huang (huanghf@scut.edu.cn).

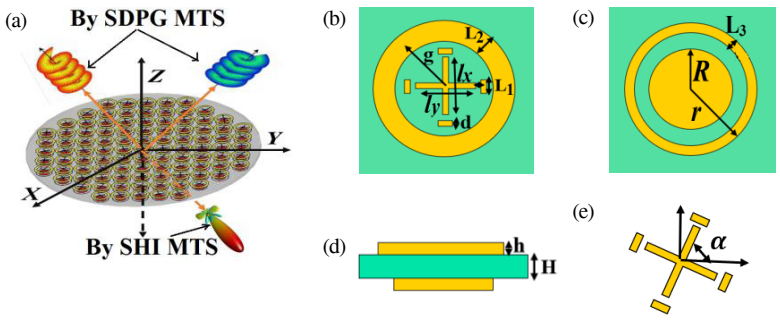

FIGURE 1. (a) Schematic diagram of the proposed SDPG-SHI hybrid MTS. For the unit: (b) top layer, (c) bottom layer, (d) Side view, (e) "+" shaped metal with rotated angle α (PB phase).

results. (3) The proposed SDPG-SHI hybrid MTS simultaneously possesses the following advantages: small size, high SHI AE 18.08%, full space, multibeams, multipolarization, reconfigurability, and simultaneous modulation of SPW and SFW. The paper is organized as follows. Section 2 is the design principle, and Section 3 is the hybrid MS design. Simulated and measured results are provided in Section 4, and Section 5 is the conclusion.

2. DESIGN PRINCIPLE

Figure 1(a) shows the schematic diagram for the SDPG-SHI hybrid MTS, which consists of three parts, the top layer metal, middle layer (F4B substrate with relative dielectric constant 2.65), and bottom layer.

2.1. The Holographic Impedance Modulation Principle for SHI MTS

In order to realize the object wave, the required scalar impedance Z of the unit cell located at $(x, y, 0)$ is derived from the interferences between objective wave $\mathbf{\Psi_{obj}}$ and excitation surface current $\mathbf{J_{surf}}$:

$$Z = j\left[\mathrm{X}+MRe\left(\Psi^*_{surf}\Psi_{obj}\right)\right] \tag{1}$$

where X and M are the average reactance and modulation index of the surface impedance and calculated as follows: $X = (Z_{max}+Z_{min})/2$ and $M = (Z_{max}-Z_{min})/2$. The excitation surface current is as follows:

$$J_{surf} = \frac{(x, y, 0)}{|\vec{r}|}e^{-j\vec{k}_t\cdot\vec{r}} \tag{2}$$

where $\vec{r}$ and $\vec{k_t}$ are the position coordinate vector and wave vector of the surface wave, respectively.

$$k_t = \sqrt{k_x^2 + k_y^2} = \sqrt{\Phi_x^2 + \Phi_y^2}/p \tag{3}$$

where Φ_x and Φ_y are the phase difference of the master-slave boundaries applied to x- and y-axis, respectively, and p is the unit cell size.

The object wave is as follows:

$$\psi_{obj} = e^{-jk_0 x sin\theta}e^{x} \tag{4}$$

By Eqs. (1), (2), and (4), and [24], a modified calculation formula for surface impedance Z of pencil beam is as follows.

$$Z = \begin{cases} j\left[X + M\cos\left(k_0 x\sin\theta - k_t r\right)\right], & x \geq 0 \\ j\left[X - M\cos\left(k_0 x\sin\theta - k_t r\right)\right], & x < 0 \end{cases} \tag{5}$$

where k_0 represents the wave number in free space.

2.2. The Propagation and PB phase Calculating Principle for SDPG MTS

A horn with 3 dB beamwidth 19.2° and gain 19 dB at position (0, 0, 230 mm) is used to excite the SDPG MTS. The phase distribution in the MTS satisfies the generation of n OAM beams, and the compensation phase $\phi(xy)$ for the unit cell at $(x, y, 0)$ is in Eq. (6):

$$\phi(x,y) = \underbrace{\frac{2\pi}{\lambda}H_{(x,y)}}_{first\ \ term} + \arg\left\{\sum_{\vec{u}_m}^{\vec{u}_n}\exp\left[j\cdot\left(\underbrace{\frac{2\pi}{\lambda}\vec{r}_{(x,y)}\cdot\vec{u}_m + l_m\times\tan^{-1}(\frac{y}{x})}_{\mathrm{sec}\,ond\ \ term}\right)\right]\right\} \tag{6}$$

where $H(xy)$ is the distance between the phase center of the horn and the unit cell, and λ is the wavelength in vacuum. The first term is the compensated phase transferring the spherical wave from the horn to the plane wave. The second term is the phase compensation for generating the mth OAM beam in direction $\overrightarrow{u_m} = (\sin\theta_m\cos\varphi_m, \sin\theta_m\sin\varphi_m, \cos\theta_m)$, and m is in the range of $1 \sim n$.

TABLE 1. Geometric parameter values of the SDPG-SHI integrated unit Cell.

Parameters	p	H	g	d	L_1	L_2	L_3	R
Value (mm)	10	3	3.5	0.1	0.4	1.3	0.2	3

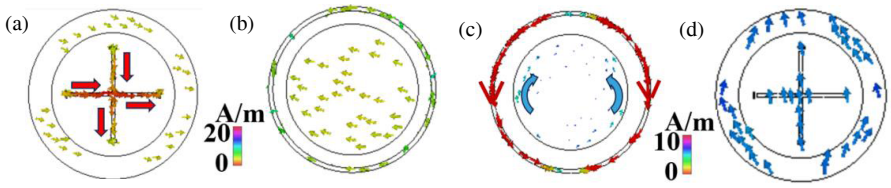

FIGURE 2. Current at 18.3 GHz for SDPG MTS unit: (a) Top side, (b) Bottom side. Current at 7.8 GHz for SHI MTS unit: (c) Bottom side, (d) Top side.

The proposed SDPG unit cell is used to implement the phase at $(x, y, 0)$ calculated by Eq. (6). Assume that the following conditions are met: $|r_x| = |r_y| = 1$, $\zeta_x - \zeta_y = \pi$, where $r_{x(y)}$ and $\zeta_{x(y)}$ are the reflection amplitude and phase (propagation phase) for the x- (y-) polarized wave, respectively. When the reflective MTS is excited by a normal circular polarization (CP) incidence, the Jones matrix of the outgoing wave is as follows [25]:

$$\begin{bmatrix} E^o_{LL} \\ E^o_{RR} \end{bmatrix} = \begin{pmatrix} e^{(\zeta_x - i2\alpha)} & 0 \\ 0 & e^{(\zeta_x + i2\alpha)} \end{pmatrix} \begin{bmatrix} E^i_L \\ E^i_R \end{bmatrix} \quad (7)$$

where E^i_L, E^i_R, E^o_{LL}, and E^o_{RR} are the LHCP and RHCP incident waves, co-polarized LHCP and RHCP outgoing waves, respectively; α is the Pancharatnam-Berry (PB) phase. From Eq. (7), the co-polarized outgoing wave is obtained, and the crosspolarized outgoing wave is suppressed. The co-polarized compensated phases at $(x, y, 0)$ for LHCP and RHCP incidences are as follows:

$$\phi_{(x,y)} = \begin{cases} \phi_{co-LHCP} = \zeta_x - 2\alpha \\ \phi_{co-RHCP} = \zeta_x + 2\alpha \end{cases} \quad (8)$$

From Eq. (6) and Eq. (8), the propagation (ζ_x, ζ_y) and PB (α) phases can be calculated by Eq. (9).

When the spin decoupling MTS is excited by LHCP or RHCP incident wave, the co-polarized reflective OAM beams are generated. Linearly polarized (LP) wave can be decomposed into two equal LHCP and RHCP waves, and the reflective beams for LP incidence are the summation of those for LHCP and RHCP incidences. When the feed polarization is switched from LHCP→RHCP→LP incidence, reconfigurable reflective waves can be generated by the spin decoupling MTS.

$$\begin{cases} \alpha = \dfrac{\phi_{co-RHCP} - \phi_{co-LHCP}}{4} \\ \zeta_x = \dfrac{\phi_{co-LHCP} + \phi_{co-RHCP}}{2} \\ \zeta_y = \zeta_x - \pi \end{cases} \quad (9)$$

3. SDPG-SHI HYBRID MTS DESIGN

As an example, the integrated SDPG part is designed for generating dual OAM beams at 18.3 GHz: (LHCP, $l_1 = 1$, $\theta_1 = 30°$, $\varphi_1 = 0°$) and (RHCP, $l_2 = 1$, $\theta_2 = 30°$, $\varphi_2 = 0°$). The integrated SHI part is designed for generating a pencil beam at 7.8 GHz: (LP, $l_3 = 0$, $\theta_3 = 150°$, $\varphi_3 = 0°$). The integrated SDPG part is excited by a horn located at (0, 0, 230 mm), and the integrated SHI part is excited by a monopole located in the MTS center. All simulated results are obtained by Computer Simulation Technology (CST).

The proposed SDPG-SHI integrated unit cell consists of three layers: top layer metal (a circular patch surrounded by a circular ring), middle layer (F4B substrate with relative dielectric constant 2.65), and bottom layer ("+" shaped metal surrounded by a circular ring). Figs. 1(b), (c), (d), (e) are the top layer, bottom layer, side view, and "+" shaped metal with rotated angle α of the integragted SDPG-SHI unit cell, respectively. All geometry parameters are marked in Fig. 1, and the optimized values are shown in Table 1. The current distributions are shown in Fig. 2. (1) For the SDPG unit at 18.3 GHz: a) In the top side, the current concentrates on the "+" shaped patch (Fig. 2(a)), so the phase is controlled by the "+" shaped patch. The propagation phase and PB phase for SDPG unit cell are controlled by geometry parameters $l_{x(y)}$ and α, respectively. b) As in Fig. 2(b), the circle ring (top side) has antiparallel current distribution with the metal (bottom side), and the effective current is in the current direction of the bottom metal, which acts as the ground for the SDPG. So the "+" shaped patch (top side) and the metal (bottom side) together act as the SDPG unit. (2) For the SHI unit at 7.8 GHz: a) In the bottom side, there is a resonance current distribution with one wavelength path in the circle ring (Fig. 2(c)), so the surface impedance is controlled by the geometry parameter r. b) The circular patch (bottom side) and the metal (top side) have antiparallel current distributions with the circle ring (bottom side) (Figs. 2(c), (d)), and act as the ground of the SHI unit part. So the circle ring (bottom side), circular patch (bottom side), and metal (top side) together act as the SHI unit. Based on the current distribution analysis, the SDPG and SHI units can be controlled independently.

To generate the object wave, the integrated SHI unit cell in Fig. 1 is used to implement the scalar impedance Z at $(x, y, 0)$

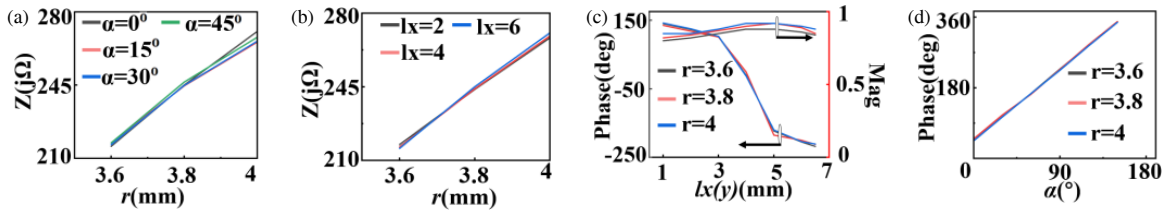

FIGURE 3. Simulated curves: (1) Surface impedance vs r at 7.8 GHz: (a) for $\alpha = 0$, $lx(y) = 2$ mm, 4 mm and 6 mm, (b) for $\alpha = 0°$, 15°, 30°, 45°, $lx(y) = 2$ mm. (2) Phase shift or S_{11} magnitude vs $lx(y)$ at 18.3 GHz for $\alpha = 0°$, $r = 3.6$ mm, 3.8 mm, 4 mm (c), PB phase vs α curves for $r = 3.6$ mm, 3.8 mm, 4 mm at 18.3 GHz (d).

calculated by Eq. (5). The equivalent impedance for the proposed unit is calculated by [26]:

$$Z = jZ_0\sqrt{1 - \frac{(\Phi_x + \Phi_y)^2 c^2}{4p^2\omega^2}} \tag{10}$$

where Z_0, c, and ω are the impedance in free space, the light speed in free space, and the angular frequency, respectively. The phase differences of the unit along the x and y directions at 7.8 GHz are $(\Phi_x, \Phi_y) = (0, 110°)$ and $k_t = 191.9$. Fig. 3 shows the curves of impedance Z (phase or S_{11} magnitude) vs the geometry parameter. For the SHI unit cell at 7.8 GHz in Fig. 3(a), the curves of impedance Z vs r overlap for $\alpha = 0°$, 15°, 30°, 45°, $l_{x(y)} = 2$ mm. In Fig. 3(b), the curves of impedance Z vs r overlap for $\alpha = 0$, $l_{x(y)} = 2$ mm, 4 mm, and 6 mm. The surface impedance Z is in the range of 215.8 Ω $\sim$ 270.7Ω when r is 3.6 mm $\sim$ 4 mm as shown in Fig. 3(a). Then, $X = 242.7$ and $M = 26.5$. The relationship between Z and r is expressed by a polynomial formula as follows:

$$Z_{e\max} = 7.55 \times 10^3 - \left(5.79 \times 10^3\right) + \left(1.49 \times 10^3\right) r^2 - \left(1.24 \times 10^2\right) r^3 \tag{11}$$

To generate the object wave, the integrated SDPG unit cell in Fig. 1 is used to implement the compensated phases (ζx, ζy, α) calculated by Eq. (9). For the SDPG unit at 18.3 GHz in Fig. 3(c) under x- (y-) polarized incidence, the curves of phase shift ($\zeta_{x(y)}$) or S_{11} magnitude vs $l_{x(y)}$ for $\alpha = 0°$, $r = 3.6$ mm, 3.8 mm, 4 mm overlap. When $l_{x(y)}$ increases from 2 mm to 6 mm, the phase shift range coving 360° is obtained, and the S_{11} magnitudes are above 0.85. Fig. 3(d) shows the PB phase vs α curves when $l_{x(y)} = 5$ mm, $r = 3.6$ mm, 3.8 mm, 4 mm. A linear relationship is observed between the PB phase and rotation angle α, and the PB phase shift covers 360° when α is from 0° to 180°. The curves in Figs. 3(a), (b) overlap for different $l_{x(y)}$ or α values, indicating that the SDPG modulation has no effect on SHI MTS. The curves in Figs. 3(c) and (d) overlap for different r values, indicating that the SHI modulation has no effect on SDPG MTS. Fig. 3 further validates that the integrated SDPG and SHI MTS functions can be modulated independently.

The SDPG-SHI integrated hybrid MTS, with size $\pi \times 118$ mm $\times$ 118 mm ($\pi \times 7.19\lambda \times 7.19\lambda$ at 18.3 GHz, and $\pi \times 3.06\lambda \times 3.06\lambda$ at 7.8 GHz) shown in Fig. 1(a), is formed by 420 unit cells. The integrated SHI MTS is designed

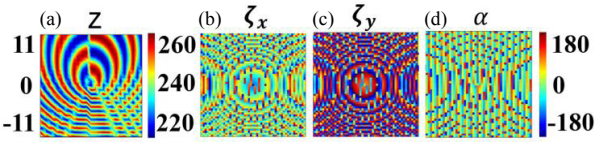

FIGURE 4. (a) The surface impedance distribution map at 7.8 GHz. The phase compensation map maps at 18.3 GHz: (b) for ζ_x. (c) for ζ_y. (d) for α.

for a pencil beam at 7.8 GHz: (LP, $l_3 = 0$, $\theta_3 = 150°$, $\varphi_3 = 0°$). The surface impedance (Z) distribution map for the SHI MTS calculated by Eq. (5) is shown in Fig. 4(a). Then according to Fig. 3(a) and Fig. 4(a), the radius r of the outer ring (bottom side) at $(x, y, 0)$ position is determined. The integrated SDPG MTS is designed for dual OAM beams at 18.3 GHz: (LHCP, $l_1 = 1$, $\theta_1 = 30°$, $\varphi_1 = 0°$), (RHCP, $l_2 = 1$, $\theta_2 = 30°$, $\varphi_2 = 0°$). The phase compensation maps for ζ_x, ζ_y, α calculated by Eq. (9) are shown in Figs. 4(b), (c), (d), respectively. Then, geometry parameter $l_{x(y)}$ is obtained according to Fig. 3(c) and Figs. 4(b), (c).

4. SIMULATED AND MEASURED RESULTS

The designed single layer hybrid MTS is fabricated. The top and bottom sides are in Fig. 5(a), and the detailed drawings of the top and bottom sides are also given. Fig. 5(b) is the measurement environment in an anechoic chamber. The integrated SDPG MTS part is excited by an LP horn with 3 dB bandwidth 18° and the gain 17 dB at (0, 0, 230 cm), and the integrated SHI MTS part is excited by by a 10 mm height monopole antenna at the center. A KEYSIGHT E5071C Vector Network Analyzer (VNA) was used to test the E-field distribution. Fig. 6 shows the radiation patterns in the far field for the SDPG integrated MTS at 18.3 GHz. Fig. 6(a) is for LHCP incidence, and an LHCP OAM beam is formed: (LHCP, $l_1 = 1$, $\theta_1 = 30°$,

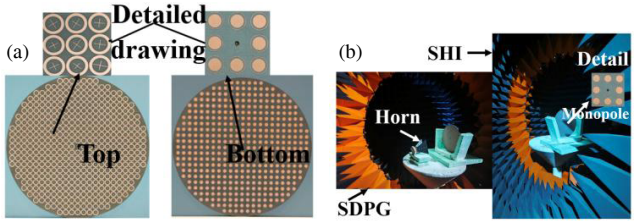

FIGURE 5. (a) The prototypes of the metasurface. (b) The measurement environment SHI function.

TABLE 2. The performance comparison between the developed SD-SHI hybrid MTS and published TM mode SHI, single layer full space MTS or hybrid single layer MTSs. (Po and Re represent polarization and reconfigurability respectively).

	MTS type	Po	mode	size	Re	AE
[11]	SHI (Half space)	CP	0	$12.5\lambda \times 12.5\lambda$	No	16.45%
[16]	SHI (Full space)	LP	0	$0.25\pi \times 3.5\lambda \times 3.5\lambda$	No	8.2% TM 25.5% TE
[21]	SHI-THI (Half space)	CP/LP	$+1/0$	$6.72\lambda \times 76.72\lambda/10.8\lambda \times 10.8\lambda$	No	14.93% SHI 23.3% THI
[20]	SHI-PG (Half space)	CP	$-1/+1$	$9.45\lambda \times 9.45\lambda/21.5\lambda \times 21.5\lambda$	No	/
[28]	THI (Full space)	LP/CP	0	$14\lambda \times 14\lambda$	No	19.8%
[27]	T-R (Full space)	LP	0	$6.67\lambda \times 6.67\lambda$	No	/
Ours	**SHI-SDPG (Full space)**	**LP/CP**	**0/±1**	$\boldsymbol{\pi \times 3.0\lambda \times 3.0\lambda/\pi \times 7.1\lambda \times 7.1\lambda}$	**Yes**	**18% SHI 13.68% SDPG**

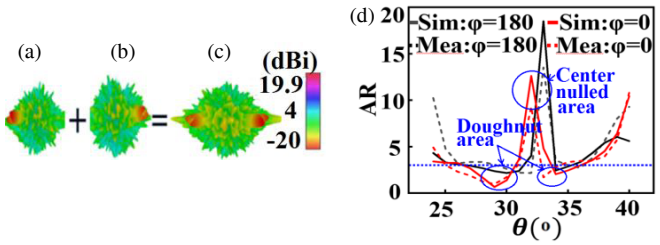

FIGURE 6. The far-field radiation patterns at 18.3 GHz of the SDPG part for different incidences: (a) LHCP, (b) RHCP, (c) LP. (d) Simulated and measured curves of AR vs θ for $\varphi = 0°$ or $180°$.

$\varphi_1 = 0°$). Fig. 6(b) is for RHCP incidence, and an RHCP OAM beam is formed: (RHCP, $l_2 = 1$, $\theta_2 = 30°$, $\varphi_2 = 0°$). Fig. 6(c) is for LP incidence, and dual CP OAM beams are formed: (LHCP, $l_1 = 1$, $\theta_1 = 30°$, $\varphi_1 = 0°$), (RHCP, $l_2 = 1$, $\theta_2 = 30°$, $\varphi_2 = 0°$). That is to say, reconfigurable reflection waves can be obtained by the SDPG MTS part when switching incidence polarization from LCP→RHCP→LP. The simulated and measured axial ratios (ARs) are given as in Fig. 6(d). The center nulled OAM area is not LHCP or RHCP (AR $>$ 3 dB), and the doughnut area of the OAM beam is CP (AR $<$ 3 dB). The linear-to-circular polarization conversion ratio (η_{cp}) is calculated according to [26], $\eta_{cp} = 2AR/(AR^2 + 1) = 95.6\%$.

Figure 7(a) is the simulated and measured far-field 2D radiation pattern for the integrated SDPG MTS part at 18.3 GHz. The simulated and measured electric field patterns are shown in Fig. 7(a). The simulated and measured gains are 19.9 dBi and 17.8 dBi, respectively, and the simulated and measured AEs are 13.6% and 8.1%, respectively. The energy density concentrates in the designed dual OAM beam directions: (LHCP, $l_1 = 1$, $\theta_1 = 30°$, $\varphi_1 = 0°$), (RHCP, $l_2 = 1$, $\theta_2 = 30°$, $\varphi_2 = 0°$), and the cross-polarization RHCP (or LHCP) component is -15 dB ~ -20 dB lower than the main beam energy density. Fig. 7(b) is the simulated E-field and phase distributions for the dual OAM beams (LHCP, $l_1 = 1$, $\theta_1 = 30°$, $\varphi_1 = 0°$), (RHCP, $l_2 = 1$, $\theta_2 = 30°$, $\varphi_2 = 0°$) in the cross section (190 mm away from the MTS along the propagation direction), and the measured results are in Fig. 7(c). The zero-intensity area in the center and helical phase pattern are clearly recognized. The phase for the LHCP beam with mode number $+1$ presents a counterclockwise spiral distribution, and the phase for the RHCP beam with mode number -1 presents a clockwise spiral distribution.

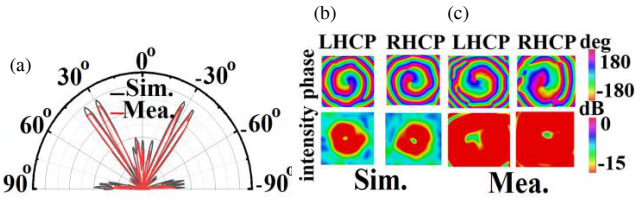

FIGURE 7. At 18.3 GHz. (1) Simulated and measured 2D radiation pattern (a), (2) The E-field and phase distributions in the cross section (190 mm away from the MTS along the propagation direction) for the dual OAM beams (LHCP, $l_1 = 1$, $\theta_1 = 30°$, $\varphi_1 = 0°$), (RHCP, $l_2 = -1$, $\theta_2 = -30°$, $\varphi_2 = 0°$): Simulated (b), and Measured (c).

According to [29], the mode purities of the vortex beams in the cross sections (190 mm away from the MTS along the propagation direction) are calculated. The simulated and measured purities for the integrated SDPG part under LP incidence are shown in Fig. 8, and are 81.9% for LHCP and 84.7% for RHCP.

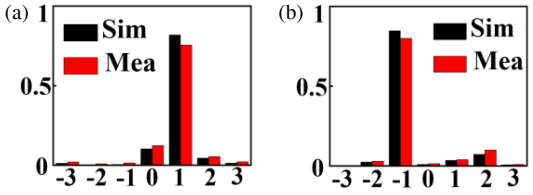

FIGURE 8. The OAM modes purity: for the LHCP OAM beam (a), for the RHCP OAM beam (b).

The simulated and measured far-field radiation patterns for the integrated SHI function part at 7.8 GHz are in Fig. 9. Fig. 9(a) is the simulated 3D radiation pattern, and Fig. 9(b) is the simulated and measured normalized 2D radiation patterns. The simulated and measured gains are 16.9 dBi and 15.8 dBi, respectively, and the simulated and measured AEs are 18% and 14%, respectively.

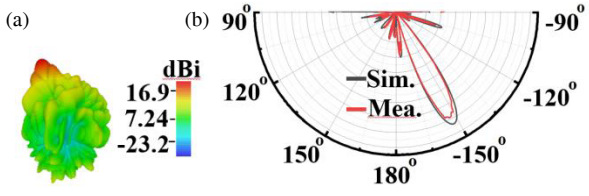

FIGURE 9. The simulated far-field radiation pattern (a), the simulated and measured normalized 2D radiation patterns (b).

Table 2 shows the performance comparison between the developed SDPG-SHI hybrid MTS and published SHI MTS, single layer full space MTS and hybrid single layer MTSs in MTS type, polarization, size, AE. The SHI part of the developed hybrid MTS has the highest AE 18%, and the AEs of [27], [16], and [21] are 16.45%, 8.2%, and 14.93%, respectively. For full space MTS, [21], [28], and [27] refer to SHI MTS (non-hybrid), tensor holographic impedance (THI) MTS (non-hybrid), and transmission and reflection integrated phase MTS, respectively. To the best knowledge of the authors, SHI-SDPG full space MTS is integrated for the first time. For hybrid MTS, [27] integrates SHI MTS (surface wave modulation) and phase gradient MTS (space wave modulation), but it only covers half-space. The proposed SDPG-SHI hybrid MTS can modulate both surface waves (SHI) and space waves (SDPG) and covers the full space. The developed SDPG-SHI hybrid MTS simultaneously possesses the following advantages: small size, high SHI AE, full space, multi-polarization, multifunction, reconfigurability, and simultaneous modulation of surface wave and space wave.

5. CONCLUSION

In this paper, an SDPG-SHI bidirectional hybrid MTS is developed, and the integrated SDPG and SHI MTSs can be modulated independently. Three beams are generated by the integrated SDPG-SHI MTS at different frequencies: (LHCP, $l_1 = 1$, $\theta_1 = 30°$, $\varphi_1 = 0°$, 18.3 GHz), (RHCP, $l_2 = -1$, $\theta_2 = -30°$, $\varphi_2 = 0°$, 18.3 GHz), (LP, $l_3 = 0$, $\theta_3 = -150°$, $\varphi_3 = 0°$,7.8 GHz). The proposed SDPG-SHI hybrid MTS simultaneously possesses the following advantages: small size ($\pi \times 7.19\lambda \times 7.19\lambda$ at 18.3 GHz, and $\pi \times 3.06\lambda \times 3.06\lambda$ at 7.8 GHz), the high SHI AE 18.08%, full space, multibeams, multipolarization, reconfigurability, and simultaneous modulation of SPW and SFW.

ACKNOWLEDGEMENT

This work was supported by the Guangdong Major Project of Basic and Applied Basic Research (2023B0303000008), the National Key Research and Development Program of China (2020YFB1807300) and State Key Laboratory of Radio Frequency Heterogeneous Integration (Shenzhen University), No. 202306.

REFERENCES

[1] Balthasar Mueller, J. P., N. A. Rubin, R. C. Devlin, B. Groever, and F. Capasso, "Metasurface polarization optics: Independent phase control of arbitrary orthogonal states of polarization," *Physical Review Letters*, Vol. 118, No. 11, 113901, 2017.

[2] You, X., R. T. Ako, M. Bhaskaran, S. Sriram, C. Fumeaux, and W. Withayachumnankul, "Mechanically tunable terahertz circular polarizer with versatile functions," *Laser & Photonics Reviews*, Vol. 17, No. 4, 2200305, 2023.

[3] Yang, W., L. Yang, B. Cai, L. Wu, S. Feng, Y. Cheng, F. Chen, H. Luo, and X. Li, "Efficiency tunable terahertz graphene metasurfaces for reflective single/dual-focusing effects based on Pancharatnam-Berry phase," *Results in Physics*, Vol. 65, 108003, 2024.

[4] Cheng, Y., R. Xing, F. Chen, H. Luo, A. A. Fathnan, and H. Wakatsuchi, "Terahertz pseudo-waveform-selective metasurface absorber based on a square-patch structure loaded with linear circuit components," *Advanced Photonics Research*, Vol. 5, No. 8, 2300303, 2024.

[5] Wang, D., L. Yang, B. Cai, L. Wu, Y. Cheng, F. Chen, H. Luo, and X. Li, "Temperature tunable broadband filter based on hybridized vanadium dioxide (VO2) metasurface," *Journal of Physics D: Applied Physics*, Vol. 58, No. 3, 035106, 2025.

[6] You, X., R. T. Ako, S. Sriram, and W. Withayachumnankul, "3D terahertz confocal imaging with chromatic metasurface," *Laser & Photonics Reviews*, Vol. 19, No. 7, 2401011, 2025.

[7] Deng, M., M. Cotrufo, J. Wang, J. Dong, Z. Ruan, A. Alù, and L. Chen, "Broadband angular spectrum differentiation using dielectric metasurfaces," *Nature Communications*, Vol. 15, No. 1, 2237, 2024.

[8] Deng, M., S. Kanwal, Z. Wang, C. Cai, Y. Cheng, J. Guan, G. Hu, J. Wang, J. Wen, and L. Chen, "Dielectric metasurfaces for broadband phase-contrast relief-like imaging," *Nano Letters*, Vol. 24, No. 46, 14 641–14 647, 2024.

[9] Huang, Z., Y. Zheng, J. Li, Y. Cheng, J. Wang, Z.-K. Zhou, and L. Chen, "High-resolution metalens imaging polarimetry," *Nano Letters*, Vol. 23, No. 23, 10 991–10 997, 2023.

[10] Ghosh, S., S. Ghosh, and C. Saha, "Polarization diversified multi beam holographic metasurface antenna for Ku band applications," in *2024 IEEE International Conference on Electronics, Computing and Communication Technologies (CONECCT)*, 1–5, Bangalore, India, 2024.

[11] Ghosh, S., P. K. Mishra, and C. Saha, "Simplified theoretical characterization on polarized beam using axially quad-sectored impedance modulated metasurface antenna," *IEEE Antennas and Wireless Propagation Letters*, 2025.

[12] Ghosh, S., I. Ghosh, S. Ghosh, H. Priyadarshnam, C. Saha, *et al.*, "Diagonally polarized dual beam holographic metasurface antenna," in *2024 IEEE Microwaves, Antennas, and Propagation Conference (MAPCON)*, 1–4, Hyderabad, India, 2024.

[13] Casaletti, M., M. Śmierzchalski, M. Ettorre, R. Sauleau, and N. Capet, "Polarized beams using scalar metasurfaces," *IEEE Transactions on Antennas and Propagation*, Vol. 64, No. 8, 3391–3400, Aug. 2016.

[14] Li, M., S. Xiao, J. Long, and D. F. Sievenpiper, "Surface waveguides supporting both TM mode and TE mode with the same phase velocity," *IEEE Transactions on Antennas and Propagation*, Vol. 64, No. 9, 3811–3819, Sep. 2016.

[15] Luukkonen, O., C. Simovski, G. Granet, G. Goussetis, D. Lioubtchenko, A. V. Raisanen, and S. A. Tretyakov, "Simple and accurate analytical model of planar grids and high-impedance surfaces comprising metal strips or patches," *IEEE Transactions on Antennas and Propagation*, Vol. 56, No. 6, 1624–1632, Jun. 2008.

[16] Li, M., S.-Q. Xiao, and D. F. Sievenpiper, "Polarization-insensitive holographic surfaces with broadside radiation," *IEEE Transactions on Antennas and Propagation*, Vol. 64, No. 12, 5272–5280, Dec. 2016.

[17] Sievenpiper, D., L. Zhang, R. F. J. Broas, N. G. Alexopolous, and E. Yablonovitch, "High-impedance electromagnetic surfaces with a forbidden frequency band," *IEEE Transactions on Microwave Theory and Techniques*, Vol. 47, No. 11, 2059–2074, 1999.

[18] Zhang, H., X. Zhang, Q. Xu, C. Tian, Q. Wang, Y. Xu, Y. Li, J. Gu, Z. Tian, C. Ouyang, *et al.*, "High-efficiency dielectric metasurfaces for polarization-dependent terahertz wavefront manipulation," *Advanced Optical Materials*, Vol. 6, No. 1, 1700773,

2018.

[19] Huang, H.-F. and J.-Y. Wang, "Switchable terahertz orbital angular momentum bessel beams based on spin-decoupled multifunctional reflective metasurfaces," *Optics Express*, Vol. 31, No. 21, 34 855–34 870, 2023.

[20] Zhang, T. Y., S. Sun, Y. Gou, H. L. Wang, H. F. Ma, and T. J. Cui, "Frequency-multiplexed holographic-reflective coding metasurface for independent controls of surface wave and spatially propagating wave," *Advanced Optical Materials*, Vol. 11, No. 10, 2202832, 2023.

[21] Huang, H. and Y. Ma, "A scalar-tensor impedance metasurface for frequency-multiplexed multifunctional orbital angular momentum beams generation," *Microwave and Optical Technology Letters*, Vol. 66, No. 4, e34144, 2024.

[22] Cai, T., G.-M. Wang, X.-L. Fu, J.-G. Liang, and Y.-Q. Zhuang, "High-efficiency metasurface with polarization-dependent transmission and reflection properties for both reflectarray and transmitarray," *IEEE Transactions on Antennas and Propagation*, Vol. 66, No. 6, 3219–3224, Jun. 2018.

[23] Movahhedi, M., M. Karimipour, and N. Komjani, "Multibeam bidirectional wideband/wide-scanning-angle holographic leaky-wave antenna," *IEEE Antennas and Wireless Propagation Letters*, Vol. 18, No. 7, 1507–1511, Jul. 2019.

[24] Yu, L., "Research on holographic tensor impedance modulated surface antenna," Ph.D. dissertation, University of Electronic Science and Technology of China, 2015.

[25] Gou, Y., H. F. Ma, L. W. Wu, Z. X. Wang, P. Xu, and T. J. Cui, "Broadband spin-selective wavefront manipulations based on Pancharatnam-Berry coding metasurfaces," *ACS Omega*, Vol. 6, No. 44, 30 019–30 026, 2021.

[26] Wang, J. and R. Yang, "Generating high-purity directive circularly polarized beams from conformal anisotropic holographic metasurfaces," *IEEE Transactions on Antennas and Propagation*, Vol. 70, No. 11, 10 718–10 723, Nov. 2022.

[27] Zhu, L., W. Zhou, L. Dong, C. Guan, G. Shang, X. Ding, S. N. Burokur, and Q. Wu, "Full space control of meta-holograms utilizing a bilayered patterned coding metasurface," *IEEE Antennas and Wireless Propagation Letters*, Vol. 21, No. 2, 322–326, 2022.

[28] Ma, X., S. Chen, J. Han, Y. Mu, H. Liu, and L. Li, "Bidirectional multi-beam with multi-polarizations tensor holographic metasurface using bilayer anisotropic elements," *Optics Express*, Vol. 32, No. 14, 24 443–24 453, 2024.

[29] Yao, E., S. Franke-Arnold, J. Courtial, S. Barnett, and M. Padgett, "Fourier relationship between angular position and optical orbital angular momentum," *Optics Express*, Vol. 14, No. 20, 9071–9076, 2006.